

# Implementation of the Coupled Channel Approximation

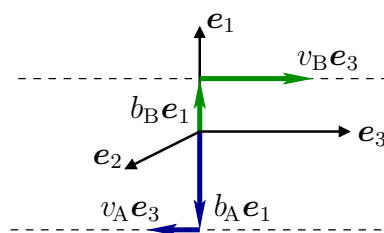
In this chapter, the capabilities of the numerical code for coupled channel calculations, which has been written for the present work, are described.

In addition, some numerical results are presented. This serves two different purposes: On one hand, the examples illustrate the principal features of the two-centre coupled channel method. On the other hand, these exemplary calculations also demonstrate the proper functioning and the correctness of the numerical software.

The entire computer code used for the numerical computations presented in this work has been newly written, except for some publicly available source code packages employed for standard tasks, like linear algebra calculations and inter-process communication in distributed computations. The general functionality, structure and algorithmic details of the program are not described in this chapter, but in appendix A.

## 5.1 Reference frames

The program does not permit to solve the coupled channel equations (4.8) in an arbitrarily chosen frame of reference, but it is the first which is capable of performing numerical computations in various different relativistic frames of reference. The coupled channel equations can be solved in such Lorentz frames, in which the centres move along the  $\mathbf{e}_3$ -axis and the centres are located on the  $\mathbf{e}_1$ -axis at time  $t = 0$ .



Hence, it is assumed in the following that the parameters  $\mathbf{b}_\Gamma$  and  $\mathbf{v}_\Gamma$  of the straight line trajectories (2.1) are given by,

$$\mathbf{b}_\Gamma = b_\Gamma \mathbf{e}_1,$$

$$\mathbf{v}_\Gamma = v_\Gamma \mathbf{e}_3,$$

where  $b_\Gamma$  and  $v_\Gamma$  are not necessarily positive.

Note, however, that the overlap and interaction matrix elements, as defined in equations (4.6) and (4.7), are invariant under spatial rotations and translations, and, therefore, the coupled channel equations in Lorentz frames connected by such Poincaré transformations are *identical*. Hence, it is true that the program allows

for the solution of the coupled channel equations in all Lorentz frames, in which the centres move on *parallel* straight-line trajectories and in which the distance of closest approach of both centres is reached at time  $t = 0$ . The particular orientation of the coordinate axes as defined above is not important.

In this chapter, primed and doubly primed coordinates are always understood as defined below:

$$\begin{aligned} t' &= \gamma_A(t - v_A x^3), & \mathbf{x}' &= (\mathbf{x} - x^3 \mathbf{e}_3) + \gamma_A(x^3 - t v_A) \mathbf{e}_3 - b_A \mathbf{e}_1, \\ t'' &= \gamma_B(t - v_B x^3), & \mathbf{x}'' &= (\mathbf{x} - x^3 \mathbf{e}_3) + \gamma_B(x^3 - t v_B) \mathbf{e}_3 - b_B \mathbf{e}_1. \end{aligned} \quad (5.1)$$

Clearly, they are rest frame coordinates of centre A and B respectively. The particular orientation of these coordinate systems later determines the angular momentum quantisation axis of coupled channel basis functions. The rapidity of centre  $\Gamma$ , a useful quantity denoted by  $\chi_\Gamma$  in the following, is related to velocity  $v_\Gamma$  by:

$$v_\Gamma = \tanh \chi_\Gamma.$$

Although numerical calculations presented in this work have been carried out for an external field originating from moving point charges, the extension of the program to arbitrary spherically symmetric charge distributions is straightforward. Thus the more general case will be considered here, in which the external field matrix  $W_\Gamma(t, \mathbf{x})$  is of the form:

$$W_\Gamma(t, \mathbf{x}) = -e V_\Gamma(r_\Gamma(t, \mathbf{x})) S(2\chi_\Gamma).$$

However,  $V_\Gamma$  is always assumed to be an attractive electrostatic potential for negatively charged electrons, such that electron bound states exist. For the matrix part  $S(2\chi_\Gamma)$  of the previous equation the abbreviation,

$$S(\chi) = \exp\left(-\frac{\chi}{2} \alpha_3\right) = \left(\cosh \frac{\chi}{2}\right) - \left(\sinh \frac{\chi}{2}\right) \alpha_3,$$

has been introduced for the boost representation matrix  $S(\chi)$ . It satisfies:

$$S(2\chi_\Gamma) = S(\chi_\Gamma)^2 = \gamma_\Gamma(1 - v_\Gamma \alpha_3).$$

The hermitian matrix  $S(\chi)$  is a real matrix in case of the standard Pauli–Dirac representation of the  $\gamma$ -matrices, used in the numerical code (see appendix C). For the present choice of reference frames, the residual external fields  $W_\Gamma^\infty(t, \mathbf{x})$ , defined in section 3.7, may be written as follows:

$$W_\Gamma^\infty(t, \mathbf{x}) = \frac{-e^2 \tilde{Z}_\Gamma}{d_\Gamma(t, \mathbf{x})} S(2\chi_\Gamma).$$

It is worth mentioning again the expressions for the Lorentz scalars  $r_\Gamma(t, \mathbf{x})$  and  $d_\Gamma(t, \mathbf{x})$ , which are defined in equations (2.4) and (2.6) and are particularly simple in the present context:

$$r_\Gamma(t, \mathbf{x}) = \sqrt{(x^1 - b_\Gamma)^2 + (x^2)^2 + \gamma_\Gamma^2(x^3 - t v_\Gamma)^2}, \quad (5.2)$$

$$d_\Gamma(t, \mathbf{x}) = \sqrt{(b_A - b_B)^2 + v^2 \gamma_\Gamma^2(t - v_\Gamma x^3)^2}, \quad (5.3)$$

Here the velocity  $v$  is given by,

$$v = \tanh |\chi_A - \chi_B|, \quad (5.4)$$

and is the relative velocity of the centres in a rest frame of either centre (cf. section 2.1). Hence, the collision energy is given by the Lorentz factor  $\gamma = \cosh(\chi_A - \chi_B)$ .

## 5.2 Spherical symmetry

The spherical symmetry of the electrostatic potential  $V_A(|\mathbf{x}'|)$  in the primed coordinates has the following well-known implications [ROS61, BD66, SAK67, THA92, EM95]. The  $t'$ -independent Hamiltonian in the primed Lorentz frame,

$$H'_A = -i\boldsymbol{\alpha} \cdot \nabla' + \beta - e V_A(|\mathbf{x}'|),$$

commutes with the spin-orbit operator,<sup>1 2</sup>

$$K' = -\beta(\mathbf{L}' \cdot \mathbf{S}' + 1), \quad (5.5)$$

and at the same time with the total angular momentum operator  $\mathbf{J}' = \mathbf{L}' + \mathbf{S}'$ . Here,  $\mathbf{L}'$  denotes the orbital angular momentum operator,

$$\mathbf{L}' = \mathbf{x}' \wedge (-i\nabla'),$$

and  $\mathbf{S}'$  the spin angular-momentum operator,

$$\mathbf{S}' = -\frac{i}{4} \boldsymbol{\alpha} \wedge \boldsymbol{\alpha}.$$

The spin-orbit operator  $K'$  commutes not only with  $H'_A$ , but also with the total angular momentum operator  $\mathbf{J}'$ . Moreover, the set of its eigenvalues  $\sigma(K')$  is the set of all nonzero integers:

$$\sigma(K') = \{\pm 1, \pm 2, \pm 3, \dots\}.$$

Due to the relation,

$$\mathbf{J}'^2 = K'^2 - \frac{1}{4},$$

any eigenfunction of  $K'$  with eigenvalue  $\kappa$  is automatically an eigenfunction of  $\mathbf{J}'^2$  with eigenvalue  $j(j+1)$ , where  $\kappa$  and  $j$  are related by:

$$j = |\kappa| - \frac{1}{2}.$$

Since  $H'_A$ ,  $K'$ , and the third component  $J'^3$  of the total angular momentum operator  $\mathbf{J}'$  form a set of commuting, self-adjoint operators, it is clear that bound states of the electrostatic potential  $V_A(|\mathbf{x}'|)$  are orthogonal, if they correspond to different eigenvalues. Any energy eigenvalue of a simultaneous eigenstate of  $H'_A$  and  $K'$ , with the eigenvalues  $\epsilon$  and  $\kappa$  respectively is at least  $2|\kappa|$ -fold degenerate, known as the angular momentum degeneracy of bound state energies for a spherical potential.

<sup>1</sup>Here the sign convention agrees with [SFVW95B].

<sup>2</sup>In principle, it is appropriate to give the operator  $K'$  (and the other operators defined in this section) an additional subscript A, in order to indicate that it is defined with respect to the primed spatial coordinates 5.1 of a rest frame of centre A. But for brevity  $K'_A$  is written simply as  $K'$ .

The energy eigenvalues, within an eigenspace of  $K'$  with eigenvalue  $\kappa$ , are commonly numbered in ascending order by an integer  $n$ , with

$$\begin{aligned} n &= |\kappa|, |\kappa| + 1, |\kappa| + 2, \dots & \text{if } \kappa < 0 \text{ and} \\ n &= \kappa + 1, \kappa + 2, \kappa + 3, \dots & \text{if } \kappa > 0. \end{aligned}$$

If degeneracies within an eigenspace of  $K'$ , that are not angular momentum degeneracies, are counted by separate indices  $n$ , then any bound state of the radially symmetric potential  $V_A$ , which is a simultaneous eigenstate of the operators  $H'_A, K'$  and  $J'^3$ , is uniquely characterised by a triple index  $(n, \kappa, m)$ . Here  $m$  denotes the eigenvalue of  $J'^3$ . However, such degeneracies do not occur for the Coulomb potential. For some potentials, like the Coulomb potential, the number of orthogonal bound states with the same eigenvalue  $\kappa$  is infinite. This number may be finite or even zero, depending on  $\kappa$ , for other attractive potentials, including the Yukawa potential and the class of potentials of equation (2.10)

Therefore, in the important case where  $V_A(|\mathbf{x}'|)$  is the Coulomb potential, *every* triple  $(n, \kappa, m)$  satisfying  $n \in \mathbb{N}$ ,

$$\begin{aligned} -n &\leq \kappa < n & \text{with } \kappa \in \mathbb{Z}, \kappa \neq 0, \text{ and} \\ |m| &\leq |\kappa| - \frac{1}{2} & \text{with } m \in \frac{2\mathbb{Z} + 1}{2}, \end{aligned}$$

corresponds to a Coulomb–Dirac bound state, which is simultaneously an eigenstate of the operators  $H'_A, K'$  and  $J'^3$ , and vice versa. These mutually orthogonal Coulomb–Dirac bound states are consecutively numbered by the single non-negative integer,

$$i = \frac{(2n-1)(n-1)n}{3} + 2\kappa^2 + \kappa + m - \frac{1}{2} = 0, 1, 2, \dots \quad (5.6)$$

This integer  $i$  constitutes the linear index for bound states, employed in numerical calculations presented in this work (see e.g. figure 5.1 on page 55). The linear ordering of Coulomb–Dirac bound states by their index  $i$  includes their partial ordering due to the energy eigenvalues. This means that  $i(n, \kappa, m) \leq i(\hat{n}, \hat{\kappa}, \hat{m})$  implies  $\epsilon_{n\kappa m} \leq \epsilon_{\hat{n}\hat{\kappa}\hat{m}}$ .

The integer  $n$  represents the principal quantum number of an eigenstate in the nonrelativistic limit of the Dirac equation and the orbital angular momentum quantum number  $l$  with respect to that limit, is given by:

$$l = \begin{cases} |\kappa| - 1 & \text{if } \kappa < 0, \\ \kappa & \text{if } \kappa > 0, \end{cases}$$

Table 5.1 lists the 28 lowest Coulomb–Dirac bound states, including their conventional spectroscopic labels. Clearly, everything described in this section applies similarly to bound states of the spherically symmetric electrostatic potential  $V_B(|\mathbf{x}''|)$  in the doubly primed Lorentz frame.

## 5.3 Basis functions

**5.3.1 Undistorted basis functions.** All basis sets of coupled channel calculations presented in this work comprise a certain number of *bound-electron* wave functions of both centre A and centre B. These basis functions are first constructed in their

TABLE 5.1. Single and triple indices of the 28 lowest Coulomb–Dirac bound states and their designations in spectroscopic notation. The integer  $i$  is defined in equation (5.6).

$i$	$n$	$\kappa$	$m$	spectrosc.
0	1	-1	$-\frac{1}{2}$	$1s_{1/2}(-\frac{1}{2})$
1	1	-1	$+\frac{1}{2}$	$1s_{1/2}(+\frac{1}{2})$
2	2	-1	$-\frac{1}{2}$	$2s_{1/2}(-\frac{1}{2})$
3	2	-1	$+\frac{1}{2}$	$2s_{1/2}(+\frac{1}{2})$
4	2	1	$-\frac{1}{2}$	$2p_{1/2}(-\frac{1}{2})$
5	2	1	$+\frac{1}{2}$	$2p_{1/2}(+\frac{1}{2})$
6	2	-2	$-\frac{3}{2}$	$2p_{3/2}(-\frac{3}{2})$
7	2	-2	$-\frac{1}{2}$	$2p_{3/2}(-\frac{1}{2})$
8	2	-2	$+\frac{1}{2}$	$2p_{3/2}(+\frac{1}{2})$
9	2	-2	$+\frac{3}{2}$	$2p_{3/2}(+\frac{3}{2})$
10	3	-1	$-\frac{1}{2}$	$3s_{1/2}(-\frac{1}{2})$
11	3	-1	$+\frac{1}{2}$	$3s_{1/2}(+\frac{1}{2})$
12	3	1	$-\frac{1}{2}$	$3p_{1/2}(-\frac{1}{2})$
13	3	1	$+\frac{1}{2}$	$3p_{1/2}(+\frac{1}{2})$

$i$	$n$	$\kappa$	$m$	spectrosc.
14	3	-2	$-\frac{3}{2}$	$3p_{3/2}(-\frac{3}{2})$
15	3	-2	$-\frac{1}{2}$	$3p_{3/2}(-\frac{1}{2})$
16	3	-2	$+\frac{1}{2}$	$3p_{3/2}(+\frac{1}{2})$
17	3	-2	$+\frac{3}{2}$	$3p_{3/2}(+\frac{3}{2})$
18	3	2	$-\frac{3}{2}$	$3d_{3/2}(-\frac{3}{2})$
19	3	2	$-\frac{1}{2}$	$3d_{3/2}(-\frac{1}{2})$
20	3	2	$+\frac{1}{2}$	$3d_{3/2}(+\frac{1}{2})$
21	3	2	$+\frac{3}{2}$	$3d_{3/2}(+\frac{3}{2})$
22	3	-3	$-\frac{5}{2}$	$3d_{5/2}(-\frac{5}{2})$
23	3	-3	$-\frac{3}{2}$	$3d_{5/2}(-\frac{3}{2})$
24	3	-3	$-\frac{1}{2}$	$3d_{5/2}(-\frac{1}{2})$
25	3	-3	$+\frac{1}{2}$	$3d_{5/2}(+\frac{1}{2})$
26	3	-3	$+\frac{3}{2}$	$3d_{5/2}(+\frac{3}{2})$
27	3	-3	$+\frac{5}{2}$	$3d_{5/2}(+\frac{5}{2})$

respective primed and doubly primed rest frames and then Lorentz-transformed into the unprimed frame of reference, where the coupled channel ansatz is made. In their rest frames the bound states are taken to be eigenfunctions of their corresponding time-independent Hamiltonians, spin-orbit operators and third component of their total angular momentum operators, as described in the previous section. Hence, these basis functions are of the form:

$$\begin{aligned}\Phi_{A,i}(t, \mathbf{x}) &= S(-\chi_A) \exp(-it' \epsilon_{A,i}) \phi_{A,i}(\mathbf{x}'), \\ \Phi_{B,j}(t, \mathbf{x}) &= S(-\chi_B) \exp(-it'' \epsilon_{B,j}) \phi_{B,j}(\mathbf{x}'').\end{aligned}\tag{5.7}$$

Here, the indices  $i$  and  $j$  refer to the linear index (5.6) of orthonormal bound state eigenfunctions of fixed energy and angular momentum. By construction, the wave functions  $\phi_{A,i}$  and  $\phi_{B,j}$  solve the following energy eigenvalue equations in their respective rest frames:

$$\begin{aligned}[-i\boldsymbol{\alpha} \cdot \nabla' + \beta - e V_A(|\mathbf{x}'|)] \phi_{A,i}(\mathbf{x}') &= \epsilon_{A,i} \phi_{A,i}(\mathbf{x}'), \\ [-i\boldsymbol{\alpha} \cdot \nabla'' + \beta - e V_B(|\mathbf{x}''|)] \phi_{B,j}(\mathbf{x}'') &= \epsilon_{B,j} \phi_{B,j}(\mathbf{x}'').\end{aligned}$$

Their precise form is not important here and given in appendix A. Although they refer to the primed and doubly primed frames respectively, the energy eigenvalues  $\epsilon_{A,i}$  and  $\epsilon_{B,j}$ , and the eigenfunctions  $\phi_{A,i}(\mathbf{x}')$  and  $\phi_{B,j}(\mathbf{x}'')$  are not primed, because eigenvalues and time-independent eigenfunctions cannot be transformed to moving frames

meaningfully, unless the external field vanishes (cf. section B.3). The boosted wave functions  $\Phi_{\Gamma,i}(t, \mathbf{x})$  of equation (5.7) solve the scattering-channel Dirac equations,

$$[H_0 + W_{\Gamma}(t, \mathbf{x}) - i\partial_t] \Phi_{\Gamma,i}(t, \mathbf{x}) = 0, \quad (5.8)$$

and will be referred to as *undistorted* basis functions, as opposed to phase-distorted basis functions introduced in the following subsection.

The specific expressions for overlap and interaction matrix elements (cf. equations (4.6) and (4.7) respectively) in the case of undistorted basis functions are presented in the following. Due to the invariance of the scalar product (discussed in section B.2), and since by construction the eigenfunctions  $\phi_{A,i}(\mathbf{x}')$  are orthonormal in the primed reference frame, the basis functions  $\Phi_{A,i}(t, \mathbf{x})$  in the unprimed reference frame are orthonormal as well for all times  $t$ . The same is true for the bound-state wave functions  $\Phi_{B,j}(t, \mathbf{x})$  of centre B. Therefore we have:

$$\begin{aligned} N_{A_j, A_i}(t) &= \delta_{ij}, \\ N_{B_j, B_i}(t) &= \delta_{ij}. \end{aligned} \quad (5.9)$$

The overlap matrix elements (4.6) between basis functions of different centres become:

$$\begin{aligned} N_{A_j, B_i}(t) &= \int \exp(it' \epsilon_{A,j} - it'' \epsilon_{B,i}) \phi_{A,j}^{\dagger}(\mathbf{x}') S(-\chi_A - \chi_B) \phi_{B,i}(\mathbf{x}'') d^3x, \\ N_{B_j, A_i}(t) &= \int \exp(it'' \epsilon_{B,j} - it' \epsilon_{A,i}) \phi_{B,j}^{\dagger}(\mathbf{x}'') S(-\chi_A - \chi_B) \phi_{A,i}(\mathbf{x}') d^3x. \end{aligned} \quad (5.10)$$

Certainly, the overlap matrix is hermitian, such that  $N_{\Delta_j, \Gamma_i}(t) = N_{\Gamma_i, \Delta_j}(t)^*$  holds, which is evident already from definition (4.6). The overlap matrix elements (5.10) are vanishing only as  $t$  approaches  $\pm\infty$  and are nonzero otherwise (cf. section 3.4).

As verified by using equation (5.8), the interaction matrix elements (4.7) between undistorted basis functions are given in the present context by the following expressions:

$$\begin{aligned} V_{A_j, A_i}(t) &= \int \left\{ -eV_B(r_B(t, \mathbf{x})) \right\} \times \\ &\quad \times \exp(it' \epsilon_{A,j} - it' \epsilon_{A,i}) \phi_{A,j}(\mathbf{x}')^{\dagger} S(-2\chi_A + 2\chi_B) \phi_{A,i}(\mathbf{x}') d^3x \\ V_{A_j, B_i}(t) &= \int \left\{ -eV_A(r_A(t, \mathbf{x})) \right\} \times \\ &\quad \times \exp(it' \epsilon_{A,j} - it'' \epsilon_{B,i}) \phi_{A,j}(\mathbf{x}')^{\dagger} S(\chi_A - \chi_B) \phi_{B,i}(\mathbf{x}'') d^3x \\ V_{B_j, A_i}(t) &= \int \left\{ -eV_B(r_B(t, \mathbf{x})) \right\} \times \\ &\quad \times \exp(it'' \epsilon_{B,j} - it' \epsilon_{A,i}) \phi_{B,j}(\mathbf{x}'')^{\dagger} S(-\chi_A + \chi_B) \phi_{A,i}(\mathbf{x}') d^3x \\ V_{B_j, B_i}(t) &= \int \left\{ -eV_A(r_A(t, \mathbf{x})) \right\} \times \\ &\quad \times \exp(it'' \epsilon_{B,j} - it'' \epsilon_{B,i}) \phi_{B,j}(\mathbf{x}'')^{\dagger} S(2\chi_A - 2\chi_B) \phi_{B,i}(\mathbf{x}'') d^3x \end{aligned} \quad (5.11)$$

Numerically the matrix elements (5.10) and (5.11) have to be evaluated by three-dimensional quadrature formulas (see appendix A). Although the interaction matrix is not hermitian, the partial symmetry  $V_{\Gamma_j, \Gamma_i} = V_{\Gamma_i, \Gamma_j}^*$  is useful to reduce the effort of the computationally very demanding numerical evaluation. The fundamental solution  $F(t, t_i)$  is then computed by integrating the differential equation (4.8) between

some suitable initial and final times,  $t_i$  and  $t_f$ , chosen in a symmetrical fashion as  $t_i = -t_f$ .

**5.3.2 Phase-distorted basis functions.** Compared to the definition (5.7) of the undistorted basis functions, the *phase-distorted* basis functions have an additional phase factor, in order to satisfy Coulomb boundary conditions. They are defined as:

$$\begin{aligned}\Phi_{A,i}(t, \mathbf{x}) &= \exp(ig_B(t, \mathbf{x})) S(-\chi_A) \exp(-it' \epsilon_{A,i}) \phi_{A,i}(\mathbf{x}'), \\ \Phi_{B,j}(t, \mathbf{x}) &= \exp(ig_A(t, \mathbf{x})) S(-\chi_B) \exp(-it'' \epsilon_{B,j}) \phi_{B,j}(\mathbf{x}'').\end{aligned}\quad (5.12)$$

We do not use different symbols for phase-distorted and undistorted basis functions, because they will not both occur in the same equation. In equations (5.12) the energy eigenvalues  $\epsilon_{A,i}$  and  $\epsilon_{B,j}$ , and the eigenfunctions  $\phi_{A,i}(\mathbf{x}')$  and  $\phi_{B,j}(\mathbf{x}'')$  are identical to those of the previous section. Although the phase-distorted basis functions are not energy or angular momentum eigenfunctions in the primed and doubly primed reference frames respectively (cf. section B.3 of the appendix), they are denoted by analogy to the undistorted functions according to table 5.1.

For the present numerical work the following gauge functions  $g_\Gamma(t, \mathbf{x})$  have been used,

$$g_\Gamma(t, \mathbf{x}) = \frac{e^2 \tilde{Z}_\Gamma}{v} \log \frac{d_\Gamma(t, \mathbf{x}) + v \gamma_\Gamma(t - v_\Gamma x^3)}{|b_A - b_B|}, \quad (5.13)$$

with  $d_\Gamma(t, \mathbf{x})$  as in equation (5.3) and  $v = \tanh |\chi_A - \chi_B|$ . Remember that  $Z_\Gamma = \tilde{Z}_\Gamma$  for the Coulomb potential. The phase-distorted basis functions (5.12) then solve the following Coulomb-distorted scattering-channel Dirac equations (cf. section 3.7):

$$\begin{aligned}[H_0 + W_A(t, \mathbf{x}) + W_B^\infty(t, \mathbf{x}) - i\partial_t] \Phi_{A,i}(t, \mathbf{x}) &= 0, \\ [H_0 + W_B(t, \mathbf{x}) + W_A^\infty(t, \mathbf{x}) - i\partial_t] \Phi_{B,j}(t, \mathbf{x}) &= 0.\end{aligned}$$

We turn to the specific expressions for overlap and interaction matrix elements in the case of phase-distorted basis functions. Since the additional phase factor cancels in scalar products between basis functions of the same centre, phase-distorted basis functions belonging to the same scattering channel are orthonormal for the same reason as above:

$$\begin{aligned}N_{A_j, A_i}(t) &= \delta_{ij}, \\ N_{B_j, B_i}(t) &= \delta_{ij}.\end{aligned}\quad (5.14)$$

The overlap between basis functions of different channels is different for undistorted and phase-distorted basis functions. The remaining elements of the hermitian overlap matrix  $N(t)$  are given by:

$$\begin{aligned}N_{A_j, B_i}(t) &= \int \exp(ig_A(t, \mathbf{x}) - ig_B(t, \mathbf{x})) \times \\ &\quad \times \exp(it' \epsilon_{A,j} - it'' \epsilon_{B,i}) \phi_{A,j}(\mathbf{x}')^\dagger S(-\chi_A - \chi_B) \phi_{B,i}(\mathbf{x}'') d^3x \\ N_{B_j, A_i}(t) &= \int \exp(ig_B(t, \mathbf{x}) - ig_A(t, \mathbf{x})) \times \\ &\quad \times \exp(it'' \epsilon_{B,j} - it' \epsilon_{A,i}) \phi_{B,j}(\mathbf{x}'')^\dagger S(-\chi_A - \chi_B) \phi_{A,i}(\mathbf{x}') d^3x\end{aligned}\quad (5.15)$$

Finally, in the case of phase-distorted basis functions the elements of the interaction matrix  $V(t)$  are explicitly:

$$\begin{aligned}
V_{Aj,Ai}(t) &= \int \left\{ eV_B(d_B(t, \mathbf{x})) - eV_B(r_B(t, \mathbf{x})) \right\} \times \\
&\quad \times \exp(it'\epsilon_{A,j} - it'\epsilon_{A,i}) \phi_{A,j}(\mathbf{x}')^\dagger S(-2\chi_A + 2\chi_B) \phi_{A,i}(\mathbf{x}') d^3x \\
V_{Aj,Bi}(t) &= \int \exp(ig_A(t, \mathbf{x}) - ig_B(t, \mathbf{x})) \left\{ eV_A(d_A(t, \mathbf{x})) - eV_A(r_A(t, \mathbf{x})) \right\} \times \\
&\quad \times \exp(it'\epsilon_{A,j} - it''\epsilon_{B,i}) \phi_{A,j}(\mathbf{x}')^\dagger S(\chi_A - \chi_B) \phi_{B,i}(\mathbf{x}'') d^3x \\
V_{Bj,Ai}(t) &= \int \exp(ig_B(t, \mathbf{x}) - ig_A(t, \mathbf{x})) \left\{ eV_B(d_B(t, \mathbf{x})) - eV_B(r_B(t, \mathbf{x})) \right\} \times \\
&\quad \times \exp(it''\epsilon_{B,j} - it'\epsilon_{A,i}) \phi_{B,j}(\mathbf{x}'')^\dagger S(-\chi_A + \chi_B) \phi_{A,i}(\mathbf{x}') d^3x \\
V_{Bj,Bi}(t) &= \int \left\{ eV_A(d_A(t, \mathbf{x})) - eV_A(r_A(t, \mathbf{x})) \right\} \times \\
&\quad \times \exp(it''\epsilon_{B,j} - it''\epsilon_{B,i}) \phi_{B,j}(\mathbf{x}'')^\dagger S(2\chi_A - 2\chi_B) \phi_{B,i}(\mathbf{x}'') d^3x.
\end{aligned} \tag{5.16}$$

Only the difference of the gauge functions  $g_A$  and  $g_B$  appears in the integrands. Note that the partial symmetry of the interaction matrix,  $V_{\Gamma_j, \Gamma_i} = V_{\Gamma_i, \Gamma_j}^*$ , holds for undistorted as well as phase-distorted basis functions.

## 5.4 Numerical tests

Before we describe in section 5.5 the inclusion of basis functions representing the scattering channel C of asymptotically free particles, some numerical calculations will be presented in this section. These results are based on a coupled channel expansion exclusively making use of bound state basis functions. Accordingly, only transition probabilities of excitation and charge transfer may be obtained by such calculations.

Numerical investigations of this kind have been carried out, and published in series of papers, by Toshima and Eichler (see the original articles [TE88B, TE88A, TE90] and also [Eic90, EM95]). The work of these authors represents the only fully relativistic two-centre coupled channel calculations available in the literature. Therefore, reproducing some of their results is an important check of the new computer program. At the same time the present work is the first independent verification of the numerical results of Toshima and Eichler.

The relativistic two-centre coupled channel calculations reported by Toshima and Eichler have been performed for a particular frame of reference, namely the *target frame*, where the initial configuration is at rest [TE88B, TE88A, TE90]. This corresponds in the present program (e.g.) to a calculation in a frame of reference, where the velocity of centre A is zero,  $v_A = 0$ , and where the initial electronic configuration is a bound state of centre A.

In figure 5.1 such a calculation is presented for a symmetrical collision of two point-like uranium nuclei, where the charge numbers are  $Z_A = Z_B = 92$ . It has been performed in a rest frame of nucleus A, with a coupled channel basis comprised of the ten lowest Coulomb–Dirac bound states of each point charge. The time-evolution of the squared moduli of the expansion coefficients  $c_{\Gamma,i}(t)$  is shown for undistorted basis functions, for an initial electronic configuration (A,  $1s_{1/2}$ ). The collision energy and

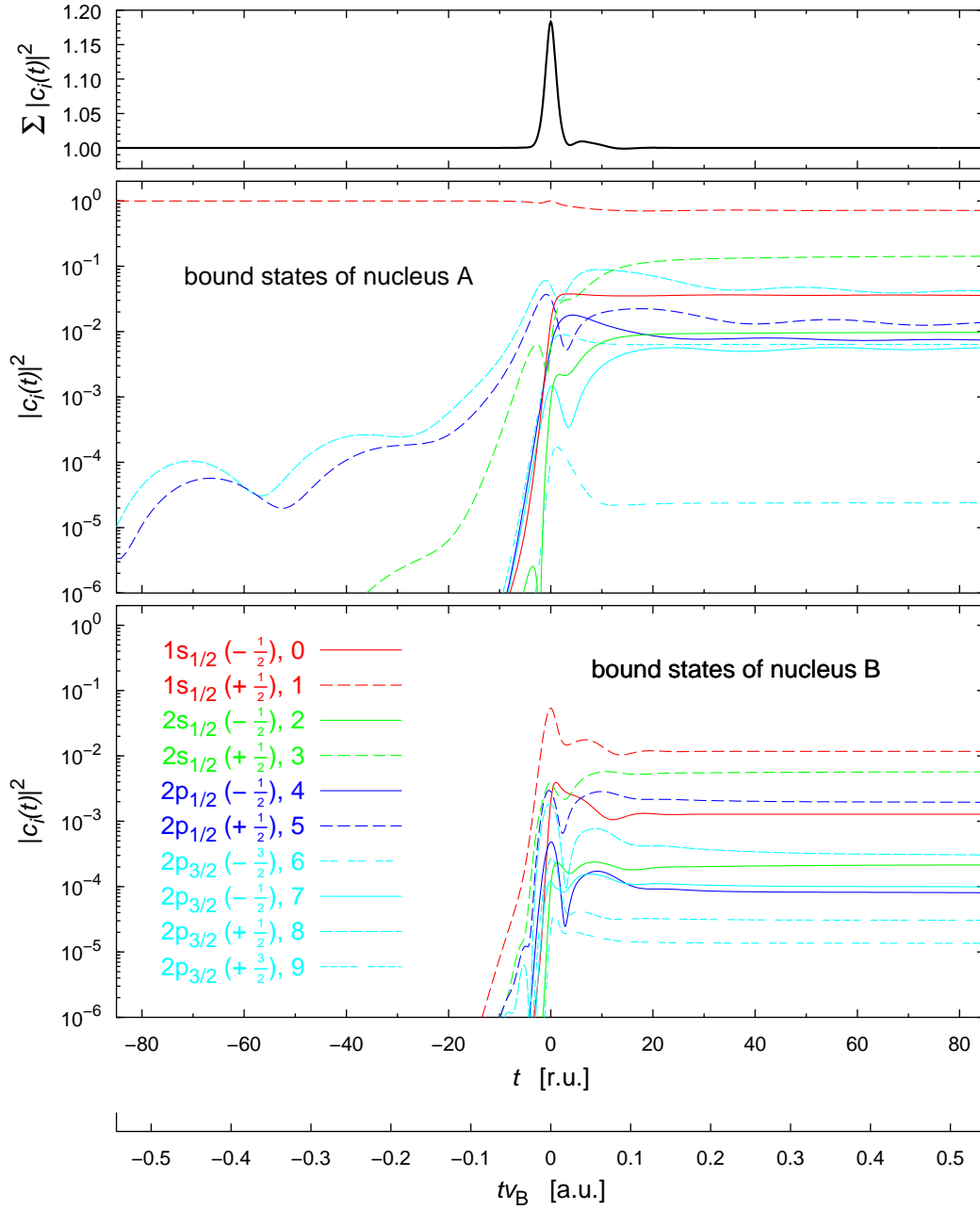


FIGURE 5.1. Time evolution of the squared moduli of the coefficients  $c_i(t)$ , as obtained from a numerical coupled channel calculation in the rest frame of nucleus A. The initial configuration presented here is  $(A, 1s_{1/2}(+\frac{1}{2}))$ . The collision energy  $T = 1 \text{ GeV/u}$  corresponds to a velocity  $v_B = 0.876 \text{ r.u.}$ . The impact parameter is  $b = 1.37 \text{ r.u.}$  or  $0.01 \text{ atomic units}$ . The charge numbers are  $Z_A = Z_B = 92$  and the ten lowest undistorted bound states have been used as basis functions. A second abscissa axis, employing atomic units, is provided to facilitate the comparison with [TE88B, figure 1]. Moreover, this second axis represents a length scale, giving the distance between the centres along the  $e_3$ -axis. Note, that the K-shell radius of nucleus A (which is not Lorentz-contracted) is approximately  $1.5 \text{ r.u.}$  or  $0.011 \text{ a.u.}$  (cf. figure 1.2 on page 9). Hence, the time interval where the K-shell radii of both centres are overlapping is small, compared to the total time axis shown here. The top plot demonstrates that the fundamental solution of the coupled channel equations is only asymptotically unitary, which implies that the sum  $\sum_i |c_i(t)|^2$  over all states of the expansion is not a constant (cf. section 4.2 and figure 5.3).

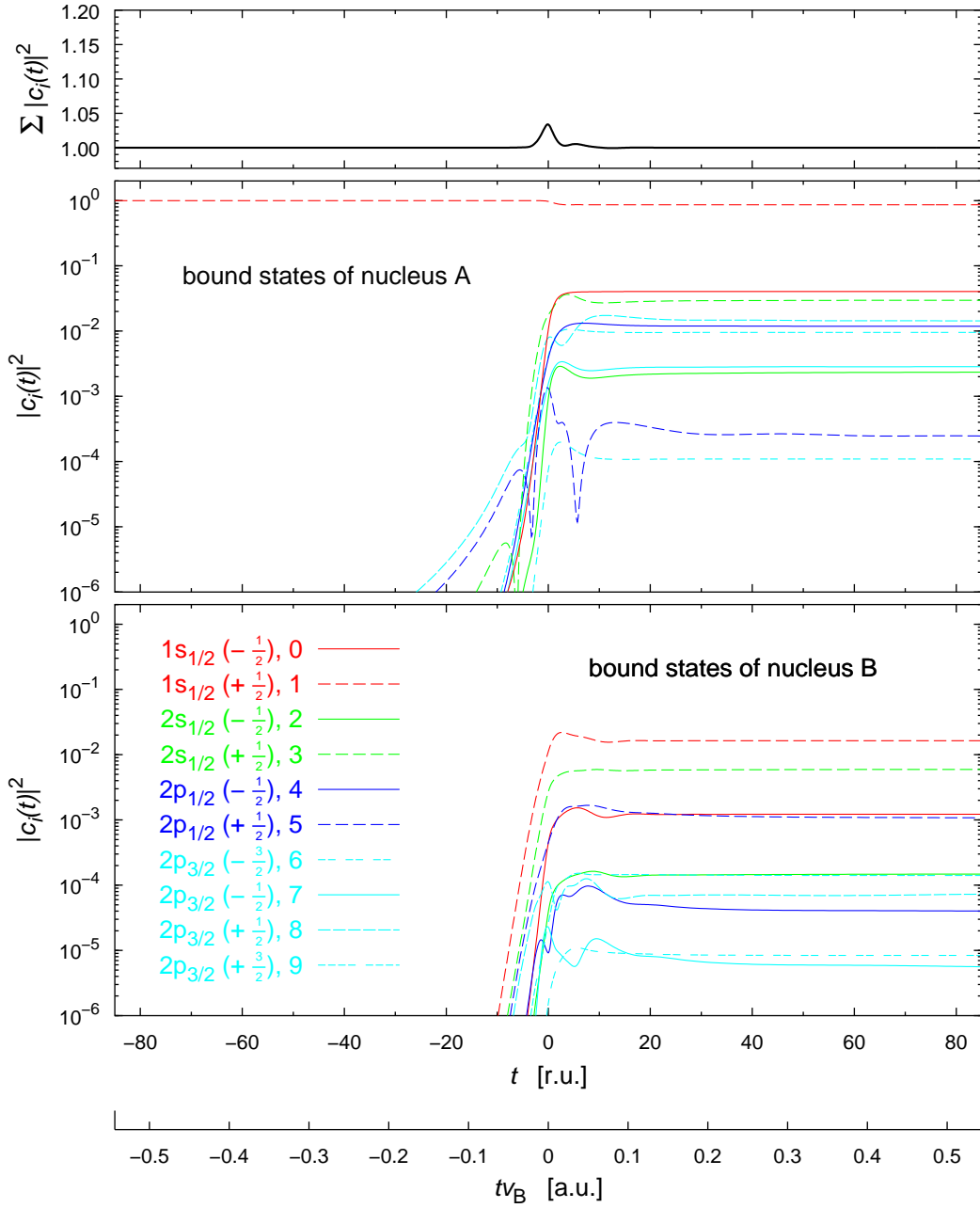


FIGURE 5.2. Time evolution of the squared moduli of the expansion coefficients  $c_i(t)$ , obtained from a coupled channel calculation with the same parameters and initial configuration as in figure 5.1, but making use of phase-distorted basis functions.

impact parameter are exactly the same as those of an analogous calculation published in [TE88B].

A comparison of the two plots at the bottom of figure 5.1 with [TE88B, figure 1] yields that their match is almost perfect. This confirms that the present numerical code is functioning properly. The numerical results published by Toshima and Eichler more than ten years ago represent an enormous achievement, in a time, when computing facilities have been much less powerful than today. The marginal difference

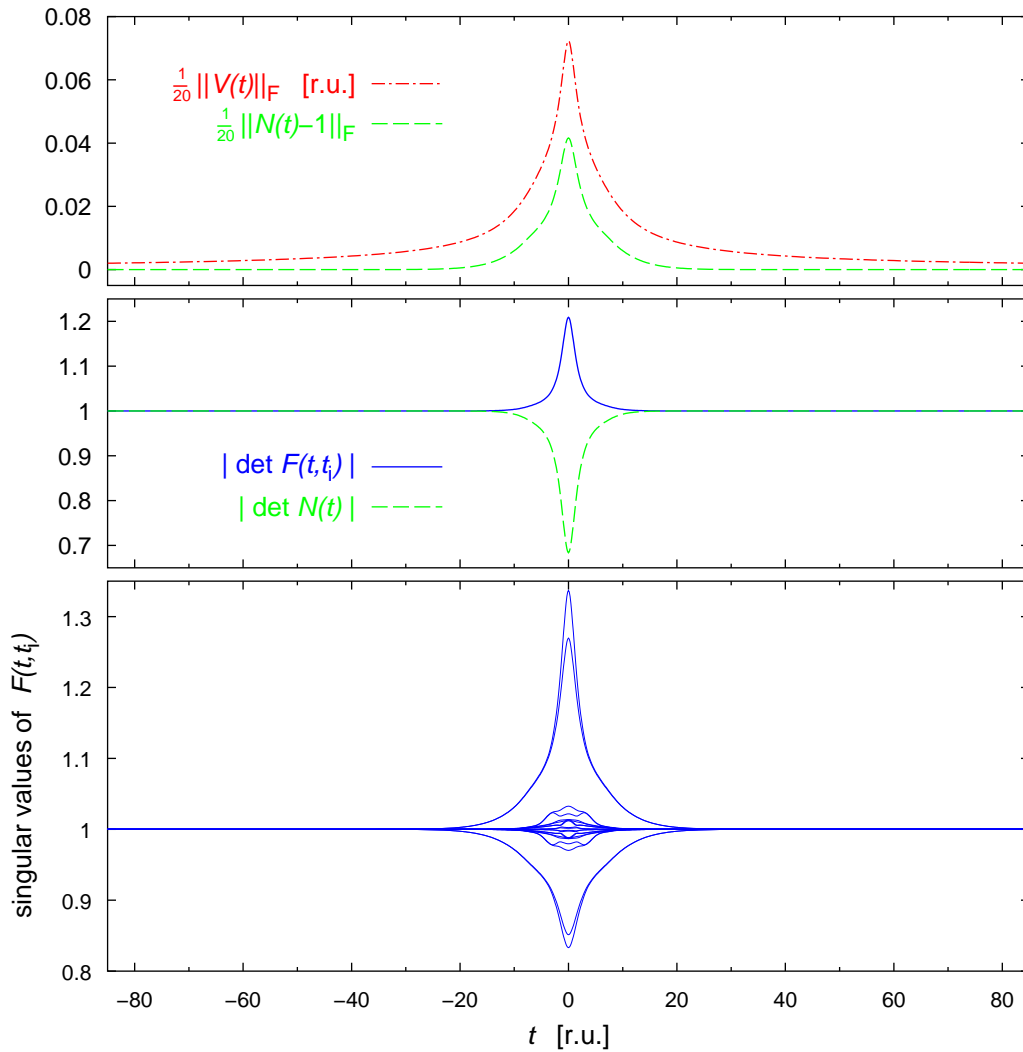


FIGURE 5.3. Properties of the overlap matrix  $N(t)$ , the interaction matrix  $V(t)$  and the fundamental solution matrix  $F(t, t_i)$  for the same calculation as shown in figure 5.1.

between the two figures is, therefore, attributed to the greater numerical accuracy of the present numerical results, due to the availability of more powerful computing facilities for the present work.

The two corresponding plots of figure 5.2 show the time-evolution of the squared moduli of the expansion coefficients, for the same collision system and parameters as in figure 5.1, with the only difference that phase-distorted basis functions have been used. In fact, the data of both figures originates from the same run of the program, which integrates the coupled channel equations for undistorted and phase-distorted basis functions simultaneously. The plot in the middle of figure 5.2 may be compared with [TE90, figure 2] or [EM95, p. 178]. The qualitative resemblance is clearly seen, although [TE90, figure 2] represents a calculation using the 18 lowest phase-distorted bound states of each centre.

A principal difference, between the plots in the middle of figures 5.1 and 5.2 respectively, is the missing excitation of target bound states in the calculation with

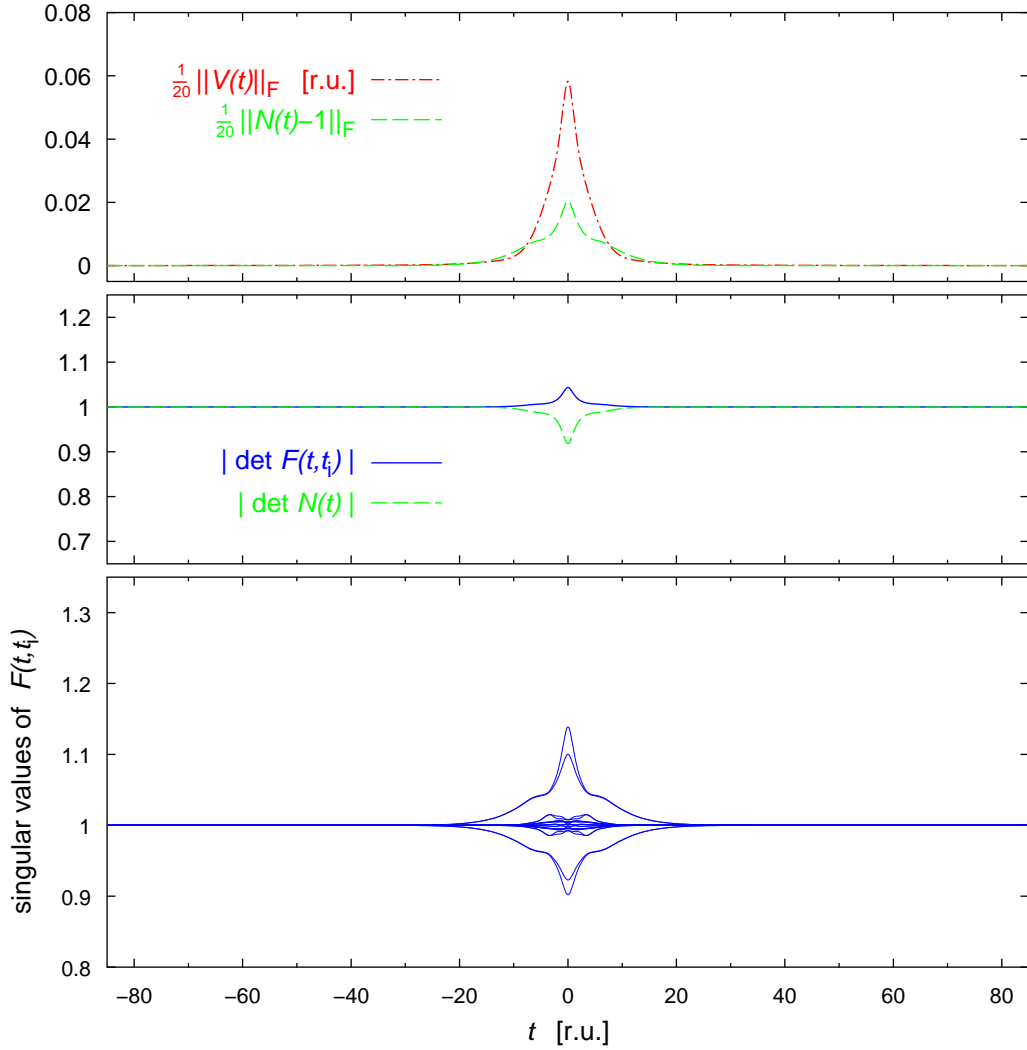


FIGURE 5.4. Properties of the matrices  $N(t)$ ,  $V(t)$  and  $F(t, t_i)$  for the numerical calculation with phase-distorted basis functions presented in figure 5.2.

phase-distorted basis functions, much before the closest approach of the centres at  $t = 0$ . It demonstrates the effect of the phase distortion, making the interaction short-ranged. In figure 5.1 the long-range character of the Liénard-Wiechert potential leads to target excitations long before the time of closest approach of the nuclei. In detail this has been described first in [TE90].

Finally, let us turn to figures 5.3 and 5.4 which illustrate typical features of the overlap and interaction matrices,  $N(t)$  and  $V(t)$ , and of the fundamental solution  $F(t, t_i)$  of the coupled channel equations, as explained in the previous section. Since these properties are known due to analytical considerations, their numerical verification constitutes another test for the numerical code. Such plots are not yet available, apparently in the quoted works the full fundamental solution has not been determined.

The green line of the top plot of figure 5.3 shows the root mean squared deviation of the overlap matrix  $N(t)$  from the unit matrix for undistorted basis functions. Up to a constant factor this root mean squared deviation is equal to the Frobenius norm

$\|N(t) - 1\|_F$  of the square matrix  $N(t) - 1$  [GV96]:

$$\|N(t) - 1\|_F = \left( \sum_{\Delta, \Gamma, j, i} |N_{\Delta j, \Gamma i}(t) - \delta_{\Delta \Gamma} \delta_{ji}|^2 \right)^{1/2}. \quad (5.17)$$

The non-orthogonality of the basis functions during the collision and their asymptotic orthonormality is properly obtained by the numerical calculation. For the existence of the inverse matrix  $N^{-1}(t)$  only the linear independence of the basis functions at any time  $t$  is necessary, which is equivalent to the regularity of the overlap matrix  $N(t)$ . This regularity of  $N(t)$  is observably provided, since the determinant  $\det N(t)$  is clearly seen to be nonzero for all times  $t$ .

The red line of figure 5.3 shows the root mean squared modulus of the interaction matrix elements, which are vanishing for large times, and are increasing towards  $t = 0$ , the time of closest approach of the centres.

In the bottom diagram of figure 5.3 the singular values of the fundamental solution  $F(t, t_i)$  are plotted as a function of time. As explained in subsection 4.2.1, the unitarity of the fundamental solution is equivalent to the property, that all singular values of  $F(t, t_i)$  are equal to one. Analytically this has been proved to hold asymptotically, and it is also obtained from the present numerical calculation for large times  $t$ . A measure of the accuracy of a numerical computation is the difference between the singular values and unity at the final time  $t_f$ .

In figure 5.4 the same quantities are presented for the calculation with phase-distorted basis functions. There are two striking differences between calculations with undistorted and phase-distorted basis functions. First, it is seen that the overlap of phase-distorted basis functions is smaller. Secondly, as  $t$  tends to  $\pm\infty$ , the interaction matrix elements decrease much faster to zero in figure 5.4 compared to figure 5.3. Again, this reflects the short-range character of the scattering theory with Coulomb-corrected, or phase-distorted, basis functions.

## 5.5 Free-particle basis functions

In order to describe ionisation and pair creation with the coupled channel method, the coupled channel basis needs to be extended by basis functions representing free particles. This section describes the basis functions chosen for the present numerical approach. Alternative basis functions, which have been used in other numerical coupled channel treatments of the two-centre Dirac equation, are discussed briefly, in order to motivate of the present choice.

**5.5.1 Free Dirac wave packets.** Free particle solutions of the two-centre Dirac equation, at least for short range forces, asymptotically approach solutions of the free Dirac equation. The time-dependent free wave packet (cf. appendix B),

$$\Phi(t, \mathbf{x}) = (2\pi)^{-\frac{3}{2}} \int e^{i\mathbf{x}\cdot\mathbf{p}} \left\{ e^{it\mu(\mathbf{p})} \hat{\phi}_+(\mathbf{p}) + e^{-it\mu(\mathbf{p})} \hat{\phi}_-(\mathbf{p}) \right\} d^3p,$$

solves the time-dependent free Dirac equation. Here  $\mu(\mathbf{p}) = \sqrt{1 + \mathbf{p}^2}$  is the free energy corresponding to the three-momentum  $\mathbf{p}$ . Therefore, in a coupled channel calculation, the free-particle scattering channel C might be represented by a finite set of free

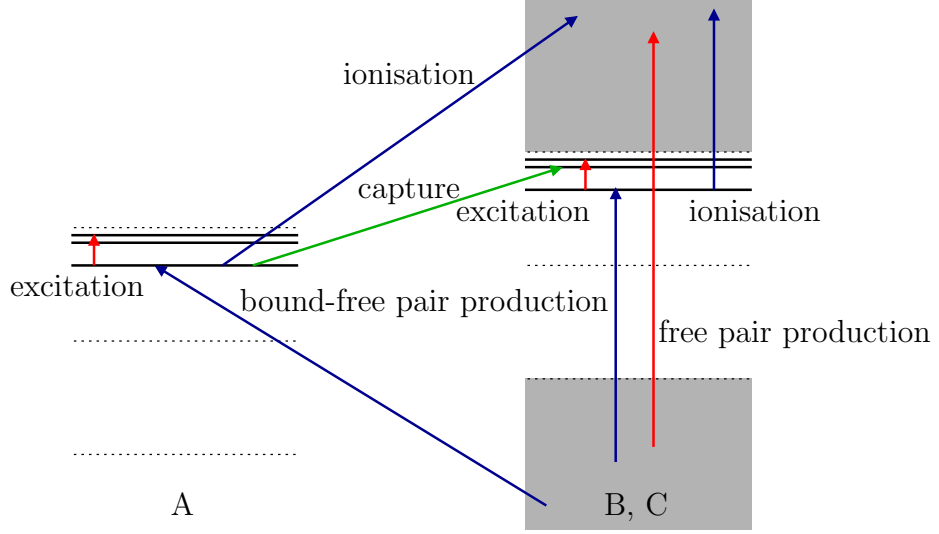


FIGURE 5.5. Asymmetrical description of the free-particle scattering channel C in a coupled channel calculation, by using wave packets of continuum eigenfunctions of centre B.

Dirac wave packets. In principle, this has been done in [THGS95, GMS<sup>+</sup>97], where the time-dependent free Dirac wave packets have been approximated by stationary wave packets, in a centre of charge frame. In these calculations the bound-state scattering channels have been omitted, such that only transition amplitudes between asymptotically free particles, in particular the free pair production amplitudes, have been obtained.

**5.5.2 Weyl eigendifferentials.** The basis functions of the coupled channel expansion (4.1) do not necessarily have to be solutions of the scattering-channel Dirac equations. In order to determine transition amplitudes it is sufficient, that the basis functions are asymptotically approaching asymptotic conditions, i.e. solutions of the scattering-channel wave equations. Such basis functions are, e.g., time-dependent wave packets constructed by means of continuum eigenfunctions of the electrostatic potential of one of the two centres. Consider for example continuum eigenfunctions  $\phi_{B,\epsilon}(\mathbf{x}'')$  of the potential  $V_B(|\mathbf{x}''|)$  in the doubly primed rest frame of centre B,

$$[-i\boldsymbol{\alpha} \cdot \nabla'' - eV_B(|\mathbf{x}''|)] \phi_{B,\epsilon}(\mathbf{x}'') = \epsilon \phi_{B,\epsilon}(\mathbf{x}''). \quad (5.18)$$

Here, the energy eigenvalue  $\epsilon$  is in the continuous spectrum  $|\epsilon| > 1$ . These continuum eigenvalues are infinitely degenerate, which is, however, not important for the moment. Time-dependent, or Weyl, wave packets of these eigenfunctions, which are Lorentz transformed into the unprimed frame, exactly solve the Dirac equation of scattering channel B:

$$[H_0 + W_B(t, \mathbf{x}) - i\partial_t] S(-\chi_B) \left\{ \frac{1}{\sqrt{\Delta_\epsilon}} \int_{\bar{\epsilon}-\Delta_\epsilon/2}^{\bar{\epsilon}+\Delta_\epsilon/2} \exp(-it''\epsilon) \phi_{B,\epsilon}(\mathbf{x}'') \, d\epsilon \right\} = 0$$

These wave packets asymptotically approach free wave packets as  $t$  goes to  $\pm\infty$ , provided that  $V_B$  is short-ranged, which is a standard result from quantum mechanical two-particle scattering theory [RS79, THA92]. Therefore, they represent asymptotically free particles. Such Weyl wave packets are clearly orthogonal to the bound

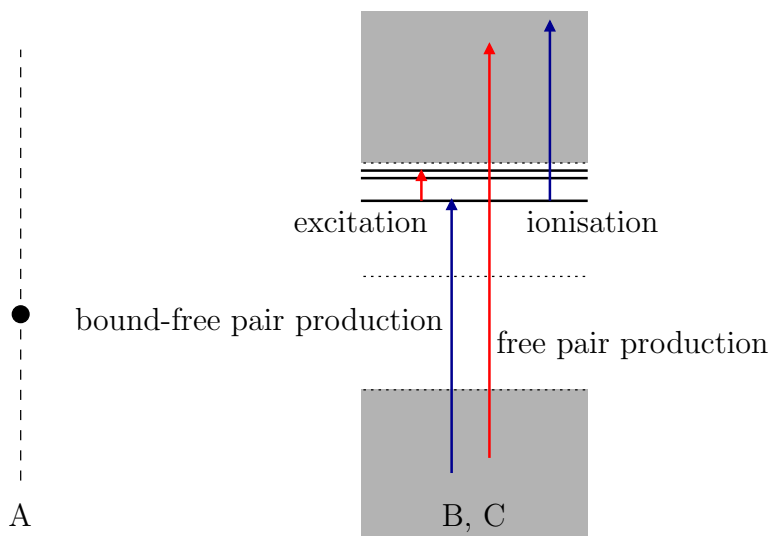


FIGURE 5.6. Asymmetrical description of the free-particle scattering channel C in a coupled channel calculation, as in figure 5.5, but here the charge transfer channel is omitted as well. Hence, centre A only acts as a perturbation.

states of centre B. The Weyl wave packets are also asymptotically orthogonal to the bound states of centre A, since they are spreading asymptotically in the same way as the wave packets of the free Dirac equation (see section 3.4). In principle, Weyl wave packets of one of the two centres may, therefore, be used as basis functions, representing the free-particle scattering channel in a coupled channel calculation. This approach is schematically depicted in figure 5.5.

The main argument, against the use of Weyl wave packets in numerical calculations, is the additional energy integration, necessary for a numerical determination of overlap and interaction matrix elements. This presents a considerable numerical complexity in practical calculations, well-known already from less demanding nonrelativistic coupled channel calculations [BM92]. Nevertheless, relativistic *single*-centre coupled channel calculations in the target frame have been done and presented in [MGS91]. There, a coupled channel basis comprising bound states of one particular centre (the target) and Weyl wave packets of the same centre have been used (cf. figure 5.6).

Clearly, the choice of centre B for the construction of the wave packets is asymmetrical. Weyl wave packets of centre A are equally suitable for the representation of the free-particle channel, at least in a symmetrical collision system. Hence, a coupled channel basis comprising a (necessarily) finite number of Weyl wave packets, of both centre A and centre B, at first glance, seems to be a more appropriate choice. But it is not clear, how to construct these wave packets such that they are asymptotically orthogonal and, moreover, the approach towards the asymptotic orthogonality is fast enough for numerical calculations. Numerical calculations using a two-centre basis comprising free-particle states of this kind have not been attempted yet.

**5.5.3 Stationary wave packets.** Weyl wave packets are obtained from continuum eigenstates of the respective electrostatic potentials of the centres A and B. Their principal advantage over free Dirac wave packets, described in the first subsection, is

that they should be more suitable for the description of a solution of the two-centre Dirac equation. This holds in particular for strong external forces, i.e. large charge numbers, or equivalently for free electrons and positrons of low kinetic energy.

As an approximation to time-dependent wave packets, stationary wave packets have been used in the literature and also for the present work. Again, as an example, consider centre B and its continuum eigenfunctions  $\phi_{B,\epsilon}(\mathbf{x}'')$  in the doubly primed rest frame as in equation (5.18). In the doubly primed frame a stationary wave packet is defined as:

$$\Phi''_{B,\bar{\epsilon}}(t'', \mathbf{x}'') = \frac{1}{\sqrt{\Delta_\epsilon}} \exp(-it''\bar{\epsilon}) \int_{\bar{\epsilon}-\Delta_\epsilon/2}^{\bar{\epsilon}+\Delta_\epsilon/2} \phi_{B,\epsilon}(\mathbf{x}'') d\epsilon.$$

It solves the time-dependent Dirac equation in the doubly primed frame approximately:

$$\left[ H''_0 - eV_B(|\mathbf{x}''|) - i\partial_{t''} \right] \Phi''_{B,\bar{\epsilon}}(t'', \mathbf{x}'') \approx 0.$$

By construction a stationary wave packet is localised around the spatial origin of the doubly primed coordinates for all times. Although stationary wave packets do not spread, they are usually considered as a helpful substitutes for Weyl wave packets. The use of stationary wave packets is sometimes referred to as the ‘discretisation of the continuum’.

For a spherically symmetric external field the continuum eigenvalues  $\epsilon$  are infinitely degenerate, since an eigenfunction  $\phi_{B,\epsilon}(\mathbf{x}'')$  may be a simultaneous eigenfunction of the spin-orbit operator  $K''$ , with any of the eigenvalues  $\kappa = \pm 1, \pm 2, \pm 3, \dots$ . Stationary wave packets are usually constructed from eigenfunctions with definite values of the angular momentum quantum numbers  $\kappa$  and  $m$ . Such wave packets, denoted by  $\Phi''_{B;\bar{\epsilon},\Delta_\epsilon,\kappa,m}(t'', \mathbf{x}'')$  are orthogonal in the doubly primed reference frame, if their energy intervals are non-overlapping or if they have different angular momenta.

The advantage of stationary wave packets over Weyl wave packets is, that the energy integration needs to be carried out only once, yielding radial wave functions, which can be tabulated for later reference. The energy integration does not need be included in every single evaluation of an overlap or an interaction matrix element. Consequently numerical computations become less demanding.

Another advantage is that the stationary wave packets of *different* centres are asymptotically orthogonal, due to their localisation at different centres. This makes a *two-centre* description of the free-particle scattering channel feasible. As a consequence of the splitting of the free-particle basis functions into two subsets, attributed to centre A and centre B respectively, ionisation and pair creation processes both can be subdivided into ‘excitation’- and ‘transfer’-type processes. This is depicted in figure 5.7.

*Single-centre* relativistic coupled channel calculations, using stationary wave packets, have been reported in [RMS<sup>+</sup>91, RSG93, BRBW93, BRBW94]. These single-centre approaches can only describe excitation-like processes, as depicted in figure 5.6, and, therefore, they even exclude the description of the charge transfer process. A relativistic two-centre coupled channel calculation, including wave packets of *both* centres, has been implemented for the first time in this work.

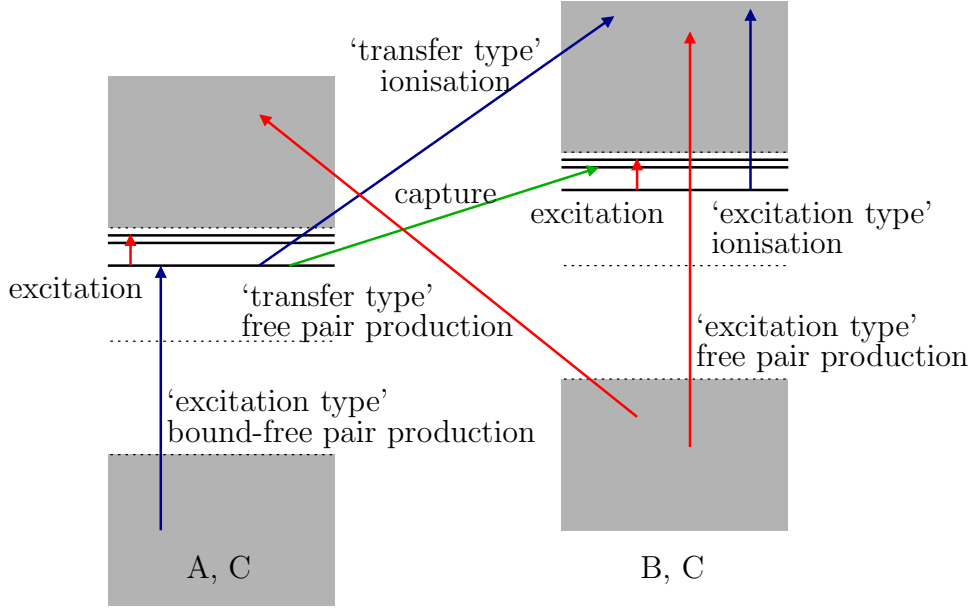


FIGURE 5.7. The two-centre approximation of the free-particle scattering channel C. Ionisation and pair creation processes may be of ‘excitation’- or ‘transfer’-type. A similar schematic picture has previously appeared in [EIC95].

**5.5.4 Details of the present approach.** Similar to bound-state basis functions, stationary wave packets for the coupled channel basis are constructed as eigenfunctions of the spin-orbit operators and the third components of the total angular momentum in the primed and doubly primed frames respectively. These wave functions have to be Lorentz-boosted into the unprimed reference frame. The parameters of such wave packets, namely the mean energy  $\bar{\epsilon}$ , the width of the energy interval  $\Delta_{\epsilon}$ , the spin-orbit quantum number  $\kappa$  and the third component of the total angular momentum  $m$ , are again abbreviated by single indices  $i$  or  $j$ . Using this notation, the additional undistorted basis functions, which have been employed in numerical calculations of the present work, have the following form in the unprimed reference frame:

$$\begin{aligned}\Phi_{A,i}(t, \mathbf{x}) &= S(-\chi_A) \frac{\exp(-it'\bar{\epsilon}_i)}{\sqrt{\Delta_{\epsilon_i}}} \int_{\bar{\epsilon}_i - \Delta_{\epsilon_i}/2}^{\bar{\epsilon}_i + \Delta_{\epsilon_i}/2} \phi_{A,\epsilon,\kappa_i,m_i}(\mathbf{x}') d\epsilon, \\ \Phi_{B,j}(t, \mathbf{x}) &= S(-\chi_B) \frac{\exp(-it''\bar{\epsilon}_j)}{\sqrt{\Delta_{\epsilon_j}}} \int_{\bar{\epsilon}_j - \Delta_{\epsilon_j}/2}^{\bar{\epsilon}_j + \Delta_{\epsilon_j}/2} \phi_{B,\epsilon,\kappa_j,m_j}(\mathbf{x}'') d\epsilon.\end{aligned}\quad (5.19)$$

The precise forms of the normalised continuum eigenfunctions  $\phi_{A,\epsilon,\kappa,m}(\mathbf{x}')$  and  $\phi_{B,\epsilon,\kappa,m}(\mathbf{x}'')$  are given in appendix A. In (5.19) the energy integrals obviously take the roles of the time-independent bound state eigenfunctions, appearing in the corresponding equations (5.7).

However, the basis functions (5.19) solve the Dirac equations of the scattering channels A and B respectively only approximately,

$$\begin{aligned}[H_0 + W_A(t, \mathbf{x}) - i\partial_t] \Phi_{A,i}(t, \mathbf{x}) &\approx 0, \\ [H_0 + W_B(t, \mathbf{x}) - i\partial_t] \Phi_{B,j}(t, \mathbf{x}) &\approx 0,\end{aligned}$$

as pointed out earlier. For the determination of the elements of the interaction matrix this fact is neglected, and the matrix elements are calculated according to equations (5.11), even if the basis function on the right hand side of the scalar product corresponds to a wave packet. This procedure is customary also for single-centre coupled channel calculations.

Unfortunately, a further drawback exists for coupled channel calculations in which the centre, a stationary wave packet is attributed to, is moving. Due to the approximation of the time-evolution of stationary wave packets in their rest frame, Lorentz-transformed wave packets of the same centre are no longer orthonormal in the unprimed frame, even if they are mutually orthogonal and normalised in their rest frame. The reason is that the Lorentz-boost invariance of the scalar product requires, that both wave functions *exactly* solve the same Dirac equation (see section B.2). Note, that such a difficulty does not exist for Weyl wave packets, because they are proper solutions of the wave equations of the respective scattering channel.

This problem has not appeared in the single-centre calculations with stationary wave packets [RMS<sup>+</sup>91, RSG93, BRBW93, BRBW94]. There, the frame of reference of the coupled channel calculation has *always* been identical to the rest frame of the centre the coupled channel basis referred to. Obviously, in a two-centre approach, at least one of the centres is moving. In practical calculations of this work the overlap matrix elements involving wave packets are evaluated numerically, using the expressions (5.10).

Also phase-distorted wave packets have been used, which are defined in the same way as the phase-distorted basis functions that represent bound states. The matrix elements with phase-distorted wave packets are also evaluated according to the equations (5.15) and (5.16). Numerical results obtained from calculations with coupled channel bases, comprising both bound-state and free-particle functions, are presented in sections 6.6 and 6.7 of the next chapter.